electronics

Article

Multi-Electrode EMG Spatial-Filter Implementation Based on Current Conveyors

Federico N. Guerrero [1,*], Valentín A. Catacora [1], Alfio Dario Grasso [2] and Gaetano Palumbo [2,*]

[1] LEICI Institute of Research in Electronics, Control and Signal Processing (UNLP-CONICET-CIC), La Plata B1900, Argentina; valentin.catacora@ing.unlp.edu.ar
[2] Dipartimento di Ingegneria Elettrica Elettronica e Informatica (DIEEI), University of Catania, I-95125 Catania, Italy; agrasso@dieei.unict.it
* Correspondence: federico.guerrero@ing.unlp.edu.ar (F.N.G.); gaetano.palumbo@dieei.unict.it (G.P.)

Abstract: In this work, a circuit topology for the implementation of a multi-electrode superficial electromyography (EMG) front-end is presented based on a type II current conveyor (CCII). The presented topology provides a feasible way to implement an amplifier capable of measuring several electrode locations and obtaining the signal of interest for posterior acquisition. In particular, a five-electrode normal double differential (NDD) EMG spatial filter is demonstrated. The signal modes necessary for the analysis of the circuit are derived, the respective rejection ratios are obtained, and the noise characteristic is calculated. A board-level electrode is implemented as a proof of concept, achieving a gain equal to 28 dB, a bandwidth of 17 Hz to 578 Hz, a noise voltage linked to the input of 3.7 μV_{rms} and a common-mode rejection ratio higher than 95 dB at interference frequencies. The topology was validated after using it as an active electrode in experimental EMG measurements with an NDD dry-contact electrode in a flexible printed circuit board.

Keywords: electromyography; EMG; double differential; current conveyor; CCII

Citation: Guerrero, F.N.; Catacora, V.A.; Grasso, A.D.; Palumbo, G. Multi-Electrode EMG Spatial-Filter Implementation Based on Current Conveyors. *Electronics* **2024**, *13*, 1735. https://doi.org/10.3390/electronics13091735

Academic Editor: Gabriella Olmo

Received: 2 April 2024
Revised: 21 April 2024
Accepted: 25 April 2024
Published: 1 May 2024

1. Introduction

Surface electromyography (sEMG) has wide applications in medical diagnosis, rehabilitation, and obtaining an alternative path of communication in EMG-based human–machine interfaces. For example, fatigue assessments can be conducted by measuring EMG signals, among other clinical applications [1–4]; hand gestures can be deduced [5]; and prostheses can be controlled by commands issued by muscle activation [6,7].

The sEMG signal can be measured using simple differential electrodes with two contacts, complex electrode arrays with a large number of electrodes, or intermediate topologies composed of multiple contacts, such as the double differential (DD) or normal double differential (NDD) configurations [8]. These latter arrangements are represented in Figure 1. Their usefulness stems from their ability to obtain an EMG output with filtered muscular crosstalk components, thereby increasing the spatial selectivity of the measurement [9–11].

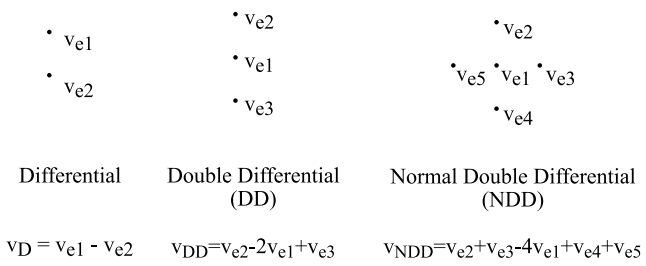

Figure 1. Surface electromyography (EMG) multi-contact topologies.

Improvements in electrode materials and support, as well as electronics miniaturization, have led to the implementation of wearable sEMG sensors in compact packages [12–15]. When the number of contacts in a stand-alone active EMG multi-electrode increases, after a certain point, it is convenient to acquire all channels individually and perform the desired function digitally using arrays, such as in structures larger than 8×8 contacts [16,17]. However, for multi-electrodes smaller than arrays, embedded as wired or wireless stand-alone acquisition elements [18,19], an analog front-end providing a weighted sum of EMG signals might deliver a convenient trade-off.

A typical case is the three-contact DD electrode and similar configurations [20–23]. However, although further spatial filtering and the isotropic characteristics of NDD electrodes can be beneficial [24,25], as the number of electrodes increases, the complexity of the analog front-end needed to perform the signal calculation grows disproportionately, thus becoming unfeasible.

Recently, Guerrero et al. proposed an efficient and practical method for acquiring EMG signals for double-differential (DD) electrodes [26]. It exploits the current mode approach and, in particular, uses a type II current conveyor (CCII) to good effect [27,28]. Indeed, the CCII circuit provides flexibility in the signal routing through its current output, allowing the implementation of a weighted sum combination of the signals using passive components and thus enabling a simple implementation of complex multi-electrode topologies.

Therefore, in this work, we hypothesized that utilizing a CCII-based topology could facilitate the development of an amplifier for multi-electrode analog front-ends with a notably simplistic structure, yet which is capable of meeting the performance requirements for EMG measurements, including low noise levels, a high common-mode rejection ratio, and effective crosstalk rejection. We present a novel design of an amplifier for a multi-electrode topology, showcasing for the first time a practical NDD electrode front-end implementation based on a CCII, along with the derivation of the associated rejection ratios. The design equations are presented along with the implementation of a proof-of-concept circuit prototype and experimental validation including in vivo measurements.

2. Methodology and Design

2.1. NDD Electrode Modes

The NDD electrode has five inputs, which are geometrically arranged as in Figure 1 and represented in the following vector:

$$\vec{v}_i = \begin{bmatrix} V_{e1} & V_{e2} & V_{e3} & V_{e4} & V_{e5} \end{bmatrix}^T \tag{1}$$

As there are five independent inputs, there are five orthogonal modes to consider. The first mode is of course the normal double differential (NDDM). Next, since the rejection of electromagnetic interference (EMI) is one of the main challenges in non-invasive biopotential measurements, and EMI appears as a common-mode (CM) signal [29], it is useful to define it as a second mode of the CM of the NDD amplifier:

$$\begin{bmatrix} V_{\mathrm{NDDM}} \\ V_{\mathrm{CM}} \end{bmatrix} = \begin{bmatrix} -4 & 1 & 1 & 1 & 1 \\ 1/5 & 1/5 & 1/5 & 1/5 & 1/5 \end{bmatrix} \vec{v}_i \tag{2}$$

For the deduction of the next modes, we first consider that the NDD electrode has a sum of double-differential modes transversal to each other, $V_{\mathrm{DD},2-4}$ in the $e2 - e4$ direction and $V_{\mathrm{DD},3-5}$ in the $e3 - e5$ direction, as depicted in Figure 2. Hence, the following vectors can be found by calculating the DD signal in these directions using the NDD electrode disposition:

$$\begin{bmatrix} V_{\mathrm{DD},2-4} \\ V_{\mathrm{DD},3-5} \end{bmatrix} = \begin{bmatrix} -2/3 & 1 & -2/3 & 1 & -2/3 \\ -2/3 & -2/3 & 1 & -2/3 & 1 \end{bmatrix} \vec{v}_i. \tag{3}$$

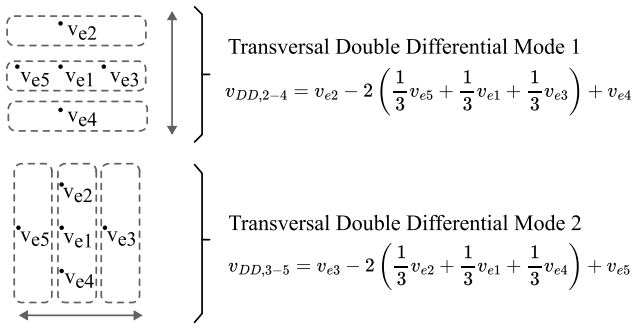

Figure 2. Depiction of the auxiliary modes from Equation (3), used in the derivation of (4).

Equation (3) defines two "averaged" DD electrodes, transversal to each other. The plane defined by these vectors contains the NDD vector $\begin{bmatrix}-4 & 1 & 1 & 1 & 1\end{bmatrix}$ as its weighted sum. Therefore, in order to find an orthogonal base for the mode decomposition, an orthogonal vector to the NDD within the same plane must be found. This vector in fact results from the subtraction of the aforementioned DD vectors; thus, we name the resulting mode the difference between transversal DD modes:

$$V_{\mathrm{DTM}} = \begin{bmatrix}0 & 1 & -1 & 1 & -1\end{bmatrix}\vec{v}_i \tag{4}$$

The rationale for the definition of the DTM is also helpful since the differential signals captured by each averaged DD electrode have crosstalk components that must be rejected, so they can be identified as modes V_{DM1} and V_{DM2}, thus completing the matrix:

$$\begin{bmatrix}V_{\mathrm{NDDM}}\\ V_{\mathrm{CM}}\\ V_{\mathrm{DTM}}\\ V_{\mathrm{DM1}}\\ V_{\mathrm{DM2}}\end{bmatrix} = \begin{bmatrix}-4 & 1 & 1 & 1 & 1\\ 1/5 & 1/5 & 1/5 & 1/5 & 1/5\\ 0 & 1 & -1 & 1 & -1\\ 0 & 1 & 0 & -1 & 0\\ 0 & 0 & 1 & 0 & -1\end{bmatrix}\vec{v}_i = M_{\mathrm{NDD}}\vec{v}_i. \tag{5}$$

In this manner, the input signal is decomposed into five modes, and the amplifier can be fully characterized by determining the transfer functions of each mode to the output, defined as follows:

$$\begin{aligned} G_{\mathrm{NDD}} &:= V_o / V_{\mathrm{NDDM}}\\ G_{\mathrm{C}} &:= V_o / V_{\mathrm{CM}}\\ G_{\mathrm{D}} &:= V_o / V_{\mathrm{DTM}}\\ G_{\mathrm{D1}} &:= V_o / V_{\mathrm{DM1}}\\ G_{\mathrm{D2}} &:= V_o / V_{\mathrm{DM2}}. \end{aligned} \tag{6}$$

The definitions in (6) allow the output equation of a practical NDD amplifier to be expressed as the superposition of all modes:

$$\begin{aligned} V_o = {} & G_{\mathrm{NDD}}V_{\mathrm{NDDM}} + G_{\mathrm{C}}V_{\mathrm{CM}}\\ & + G_{\mathrm{D1}}V_{\mathrm{DM1}} + G_{\mathrm{D2}}V_{\mathrm{DM2}} + G_{\mathrm{D}}V_{\mathrm{DTM}}. \end{aligned} \tag{7}$$

Consequently, as the only mode of interest is the NDDM, the amplifier must reject all other components, and its ability to do so can be quantified by figures of merit defined as:

$$\begin{aligned} \mathrm{CMRR} &:= G_{\mathrm{NDD}} / G_{\mathrm{C}}\\ \mathrm{DM1RR} &:= G_{\mathrm{NDD}} / G_{\mathrm{D1}}\\ \mathrm{DM2RR} &:= G_{\mathrm{NDD}} / G_{\mathrm{D2}}\\ \mathrm{DTMRR} &:= G_{\mathrm{NDD}} / G_{\mathrm{DT}}. \end{aligned} \tag{8}$$

The CMRR is analogous to its counterpart in a traditional differential amplifier and helps identify the components of the common mode (CM) that interfere with the mode of interest, in this case, the NDDM. While in a differential amplifier there are only two modes and only one rejection ratio suffices, in the NDD amplifier, there are five modes and thus additional rejection ratios are needed: the DM1RR and DM2RR quantify the rejection of both differential modes to the output, while the DTMRR measures the rejection of the difference between transversal DD modes.

It is worth noting that while the CM contains large-amplitude interference signals (typically electromagnetic interference from external sources), the other interfering modes (DM1, DM2, and DTM) capture locally generated bioelectric signals. Indeed, the traditional method of measuring EMG involves placing a differential or double-differential electrode (see Figure 1) at the measurement site. The NDD electrode will capture these same EMG signals as components of the full input signal, but it must reject them since it must produce only the NDDM at its output. Therefore, the CMRR must be high enough to reject EMI present in the CM, as in a traditional biopotential amplifier, while the DM1RR, DM2RR, and DTMRR have less challenging requirements of rejecting EMG signal components.

2.2. Circuit Topology

In previous work by the authors [26], an extension of the CCII-based instrumentation amplifier was found, highlighting that a passive network could perform the double-differential calculation in current mode. A generalization of this characteristic can be found by examining the network in Figure 3a, for which the Thévenin equivalent impedance of the electrodes can be found for the case $Z_2 = Z_3 \ldots = Z_n$ as:

$$Z_{th} = \frac{Z_n}{n-1}. \tag{9}$$

Under this condition,

$$i_1 = \left(\frac{\sum v_{ei}}{n-1} - v_{e1} \right) \frac{1}{Z_n/(n-1) + Z_1} \tag{10}$$

which yields, for the case of the NDD electrode where $n = 5$:

$$\begin{aligned} i_1 &= \frac{1}{4} \left(\sum_2^5 v_{ei} - 4v_{e1} \right) \frac{1}{Z_n/4 + Z_1} \\ &= \frac{v_{NDD}}{4} \frac{1}{Z_n/4 + Z_1}. \end{aligned} \tag{11}$$

The current through Z_1 is thus the NDD signal affected by a configurable transfer function dependent on the network impedances in the ideal condition of perfectly matched impedances Z_{2-5}. Therefore, from (11), we can implement an NDD electrode by measuring the current through Z_1 by using a CCII, as shown in Figure 3b.

The CCII is a three-terminal circuit whose nodes are labeled X, Y and Z, with the currents and voltages at these nodes related by the following equation [28]:

$$\begin{bmatrix} v_x \\ i_y \\ i_z \end{bmatrix} = \begin{bmatrix} 0 & 1 & 0 \\ 0 & 0 & 0 \\ \pm 1 & 0 & 0 \end{bmatrix} \begin{bmatrix} i_x \\ v_y \\ v_z \end{bmatrix}, \tag{12}$$

where the + and − signs in the matrix are used for positive (CCII+) and negative type (CCII−) conveyors, respectively, according to whether the output current flows in the same direction of the X node current.

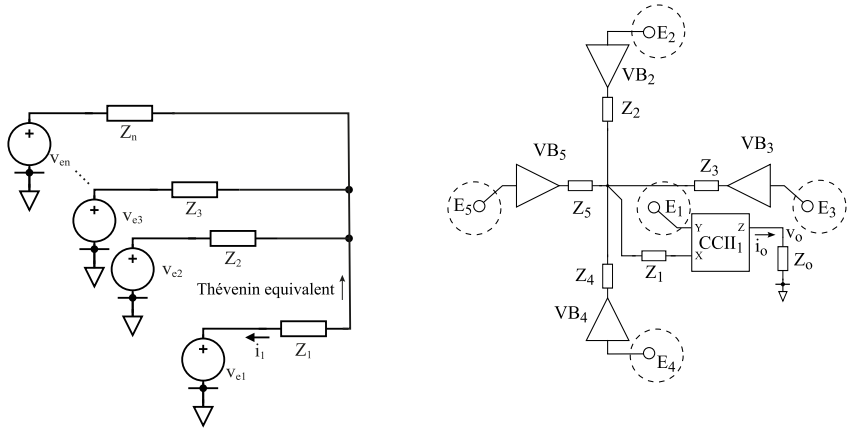

Figure 3. (**a**) Simplified equivalent circuit for input–output transfer calculation. (**b**) Circuit implementation for NDD electrode. VB stands for "voltage buffer".

Thus, according to the proposed topology in Figure 3b, applying the voltages of electrode E_1 to the CCII Y node, we determine the current through Z_1 (connected to the CCII X node), which, as stated by (12), is replicated in the output of the CCII Z node. In conclusion, from (11) and considering the load, Z_o, at the CCII Z node, we obtain:

$$v_o = \frac{v_{NDD}}{4} \frac{Z_o}{Z_n/4 + Z_1} \tag{13}$$

and hence:

$$G_{NDD} = \frac{Z_o}{Z_n + 4Z_1} \tag{14}$$

2.3. Rejection Ratios

Each signal mode in the topology can interfere with the NDDM through some mode transformation mechanism; hence, the rejection ratios must be analyzed. In the context of biopotential measurements, the most demanding rejection ratio is the CMRR since large-amplitude power-line interference signals are present in the CM [29].

The main sources of CMRR degradation are typically an imbalanced input impedance [30]. In the proposed topology, a buffer (or CCII input terminal X which is buffered) is connected to every electrode; hence, a balanced input stage is provided. Other imbalances which affect the CMRR are due to both the open-loop gain A_{ol} of the buffers and their CMRR. Finally, non-idealities from the CCII can introduce further unwanted mode transformations, mainly due to $G_{mf} = i_Z/v_Y$ [31], which causes an output current component which also depends on the voltage of the input Y node (instead of it being purely dependent on the output current of node X).

One key feature of the presented topology is that although it relies on a passive averaging network to perform the NDD calculation, imbalances in these impedances do not affect the CMRR and only affect the figures of merit DM1RR, DM2RR and DTMRR.

The above assertion can be demonstrated by expanding (11) for the case where all impedances are not equal. Remembering that the NDDM is in fact the sum of two DDMs, the values of each impedance can be expressed in terms of Z_1 and imbalances Δ_a to establish the difference between the two DD sets (Z_{2-1-4} and Z_{3-1-5}), and Δ_b and Δ_c

for the differential imbalance within each DD set (Z_2 vs. Z_4 and Z_3 vs. Z_5, respectively), so that:

$$Z_2 = Z_1 + \Delta_a + \Delta_b \qquad Z_4 = Z_1 + \Delta_a - \Delta_b$$
$$Z_3 = Z_1 - \Delta_a + \Delta_c \qquad Z_5 = Z_1 - \Delta_a - \Delta_c \tag{15}$$

which leads to expressing the output current i_o as

$$i_o = \gamma(Z_2 Z_4((Z_1 - \Delta_a)v_{DD1} + \Delta_c v_{D1}) + Z_3 Z_5((Z_1 + \Delta_a)v_{DD2} + \Delta_b v_{D2})). \tag{16}$$

where γ is a proportionality factor that depends only on the impedances.

Equation (16) shows that even when considering the full set of possible unbalances, the output current does not depend on the CM, which carries large interference components. Moreover, because DM1, DM2 and DTM only carry EMG signals, the requirements for the corresponding rejection ratios are far less demanding than for the CM [30], and a rejection of 40 dB is enough to reduce interference from these modes to 1 %, which is easily achievable with commercial passive components.

2.4. CCII and Proof-of-Concept Implementation

In order to test and validate the proposed topology, a proof-of-concept circuit was realized. However, in order to realize a board-level implementation, instead of a CCII circuit, which is not easy to find as an off-the-shelf component, a surrogate has been used. In particular, noting that since the output taken from the CCII amplifier is the voltage on impedance Z_o (due to the output current from the CCII Z node), we can achieve the same result by using an operational amplifier (OA) connected as in Figure 4a, which implements an equivalent function to the CCII [26]. Indeed, thanks to the virtual ground property, the voltage v_i at the OA non-inverting input is accurately replicated at the OA inverting input, as occurs in the CCII at nodes Y and X. Moreover, the current produced at the OA inverting node when a load is connected is exactly the current that crosses the Z_o impedance, again, like in a CCII (Figure 4a).

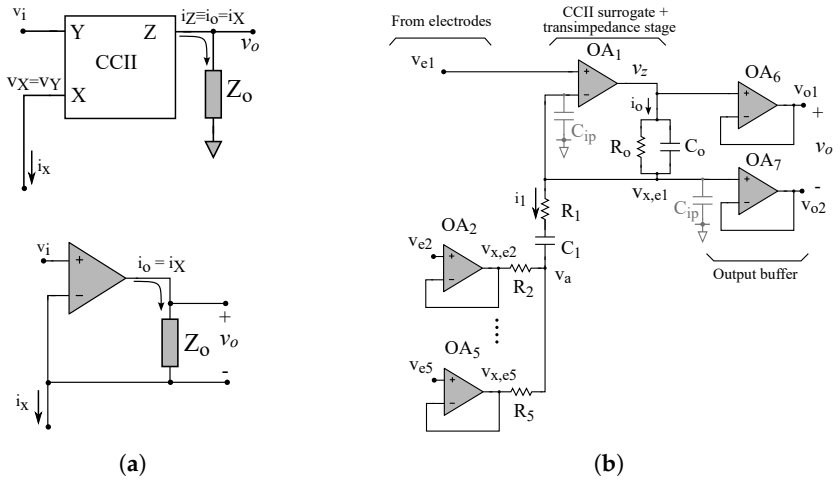

Figure 4. Implementation of an active electrode built to validate the proposed topology. (**a**) Equivalent CCII made up with an OA. (**b**) Full schematic of the active electrode, where parasitic components are marked in gray.

By using the CCII surrogate, shown in Figure 4a, and OAs with a unity–gain feedback configuration for the voltage buffers VB_{2-5}, the topology in Figure 3b can be implemented with the circuit in Figure 4b. Specifically, the schematic shown in Figure 4b also includes output voltage buffers for the patient cables, thus representing a complete circuit to realize a board-level active electrode for biopotential measurements. The circuit that allows for

testing the proposed topology can be implemented using just two quadruple OAs, leaving one of the OAs free.

The output impedance Z_o was implemented with R_o and C_o to implement a low-pass filter and Z_1, to realize a high-pass characteristic, was implemented with R_1, and C_1. Indeed, a full first-order EMG band-pass filter can be obtained by implementing $Z_1 = R_1 + 1/(sC_1)$ and $Z_o = (1/R_o + sC_o)^{-1}$ and setting $Z_{2-5} = R_{2-5} = R_1$, thus having the following transfer function:

$$G_{DD} = \frac{v_o}{v_{NDD}} = \frac{1}{5}\frac{R_o}{R_1}\frac{1}{s\tau_0 + 1}\frac{s\tau_h}{s\tau_h + 1} \tag{17}$$

where $\tau_o = R_oC_o$ and $\tau_h = R_1C_1\,5/4$. Note that as the time constants are independent, a filter with a simple design results.

2.5. Noise Analysis

The dominant noise source in the proposed NDD implementation is due to the voltage noise of the voltage buffers. Hence, considering that each buffer has an independent noise source, the total output noise e_{no} can be obtained by the quadratic sum of all sources. Moreover, in the cases like the considered implementation, where all the buffers are realized with the same device, the noise sources e_n can be considered as being of equal value.

The noise sources at the input of the buffers produce a current at the output that is again transformed into a voltage by Z_o. Thus, let us distinguish the effect of the buffer for v_{e1}, which produces a current i_{n1} from the other four buffers in the topology, which, due to their symmetry, will contribute with equal currents that are named i_{n2} for brevity.

These considerations yield:

$$\begin{aligned} e_{no}^2 &= (i_{n1}Z_o)^2 + 4(i_{n2}Z_o)^2 = (Z_o)^2\left(\left(\frac{e_n}{Z_1 + Z_n/4}\right)^2 + 4\left(\frac{1}{4}\frac{e_n}{Z_1 + Z_n/4}\right)^2\right) \\ &= (Z_oe_n)^2\frac{5}{4}\left(\frac{1}{Z_1 + Z_n/4}\right)^2. \end{aligned} \tag{18}$$

Therefore,

$$e_{no} = 2\sqrt{5}G_{NDD}e_n \tag{19}$$

$$e_{ni} = 2\sqrt{5}e_n \tag{20}$$

3. Measurement Results

The implemented circuit is shown in Figure 5a. The circuit was implemented using the components and values shown in the "Component selection" section of Table 1. The values were calculated for standard EMG measurements and their resulting values are presented in the "Parameters" section of Table 1.

For experimental biopotential measurements, the electrode contacts were connected using a flexible printed circuit board (PCB), allowing the NDD geometry to be maintained while adapting to the curved shapes of the body, thus helping to avoid artifacts, as shown in Figure 5b,c. While advanced methods are actively being developed in the literature to achieve high-quality wearable electronics [32], this simple method was employed to overcome the limitation of mounting electrodes on a rigid support and to validate the proposed amplifier. However, no specific evidence was collected to assess the accuracy and stability of this electrode structure. The electrodes and their support, as depicted in Figure 5, occupied a segment measuring 30 mm by 25 mm, with an inter-electrode separation of 10 mm (Figure 5b). The circuit was implemented on a 40 mm by 40 mm PCB area, with no efforts made to optimize its size.

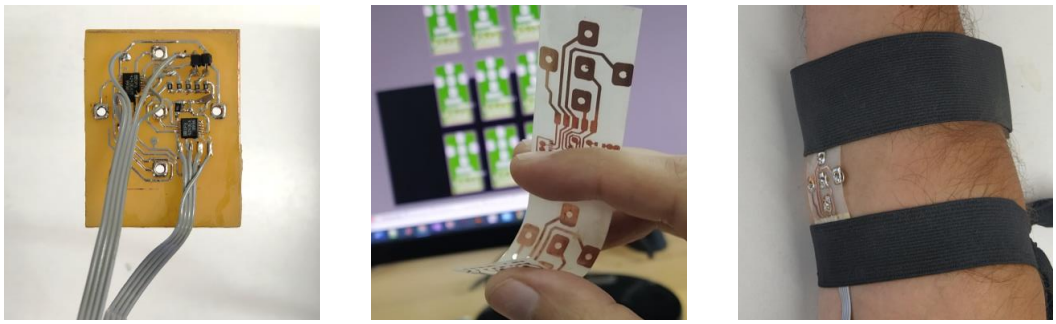

(**a**) (**b**) (**c**)

Figure 5. (**a**) Photograph of the implemented circuit board with additional wires for individual electrode measurements. (**b**) Flexible PCB with electrode connectors. (**c**) Flexible PCB with soldered dry electrodes placed on the arm.

Table 1. Implementation component list and parameters.

Component Selection		Parameters	
OA_{1-7}	2 × OPA4243	DD Gain	27.9 dB
R_1, C_1	1 kΩ, 10 µF	Bandwidth	12–578 Hz
R_{2-5}	1 kΩ	RTI noise 30–450 Hz	3.7 μV_{rms}
R_o, C_o	125 kΩ, 2.2 nF	CMRR @ 50 Hz	95.6 dB
		DC Input range	Rail-to-Rail
		Supply	326 µA, 5 V or 3.3 V

To measure the parameters of the NDD electrode using standard instrumentation, the input was first adapted by short-circuiting the four outer electrodes together ($e2 - e5$), forming an input v_{di} between nodes v_{e1} and v_{e2-e5}, where the latter were connected to a reference voltage so that $\vec{v_{di}} = (\begin{bmatrix}1 & 0 & 0 & 0 & 0\end{bmatrix})^T v_{di}$. This excitation signal in fact has two superposed modes; hence, measuring the output yields

$$\begin{aligned} v_o &= \begin{bmatrix} G_{NDD} & G_C & G_{D1} & G_{D2} & G_{TDD} \end{bmatrix} M_{NDD}\, \vec{v_{di}} \\ &= -4\, G_{NDD}\, v_{di} + \frac{1}{5}\, G_C\, v_{di} \\ \therefore\ G_{NDD} &\approx -\frac{1}{4}\frac{v_o}{v_{di}} \end{aligned} \tag{21}$$

which allows measuring G_{NDD} in the relevant frequency band where $G_{NDD} >> G_C$. With this configuration, it is possible to use a standard spectrum analyzer to obtain the frequency response applying a correction factor of four times from (21) in post-processing.

A comparison of the theoretical and experimental results of the NDD electrode's gain is shown in Figure 6a, where a high accuracy between the measured and the calculated curve is apparent, thus validating the presented Equation (17).

The common-mode gain can be measured in a direct way by short-circuiting all inputs together to a signal source. In particular, an INA111 instrumentation amplifier with a gain of 100 was used at the output of the circuit. The G_C curve was measured and the scale was adjusted to account for the added gain in post-processing. The numerical G_{NDD} curve was adjusted to the measured G_{NDD} to be able to calculate the CMRR.

The CMRR measurement is shown in Figure 6b, where it is seen to achieve a 95 dB level for the fundamental power-line interference frequency of 50 Hz and a level above 90 dB for the first five harmonics as well.

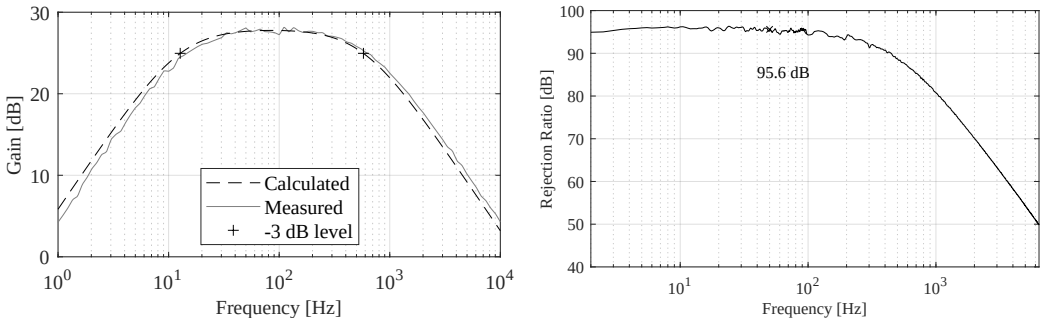

(**a**) (**b**)

Figure 6. Measured curves. (**a**) Normal double-differential gain. (**b**) CMRR.

Noise was measured by short-circuiting all inputs to a common reference voltage and capturing a 60 s signal within a shielded enclosure. The measured signal was band-pass filtered between 30 and 450 Hz and divided by the NDD gain to obtain the RTI noise v_{ni}. The integrated noise was 3.7 μV_{rms}, referred to the NDD input. The noise equations were verified by calculating the spectral amplitude of v_{ni} from the measured output noise applying the inverse of the NDD gain from (17), and in parallel by applying (20) to a measurement of the noise of a single buffer. A simulation of the system obtained using the SPICE model provided by Texas Instruments, performed using TINA software (version 9.3, from Texas Instruments), was also obtained. The results are shown in Figure 7, where a high agreement between experimental and simulated results is apparent.

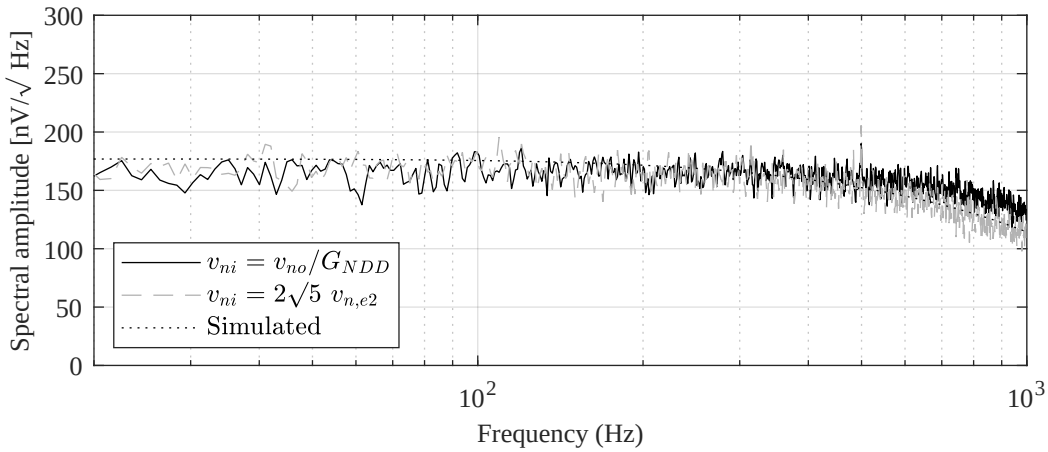

Figure 7. RTI noise spectral amplitude.

Finally, in vivo biopotential measurements were conducted using the implemented active electrode. The differential output signal carrying the NDDM was connected to a previously reported acquisition system based on an ADS1299 24-bit analog-to-digital converter (ADC) with eight differential channels. Extra cables were connected to nodes $v_{x,e1}$ to $v_{x,e5}$ and routed to channels 2 to 6 of the ADC to capture the potentials at each node.

The results from EMG measurements are shown in Figures 8 and 9. In particular, Figure 8 displays three short contractions of the wrist. The signal was scaled to account for the electrode gain.

In order to validate the NDD function of the electrode, the correlation between the output and a digitally obtained NDD signal was determined, and the correlation coefficient was 0.98. The signal source for this calculation is the segment shown in Figure 9a, consisting of a longer contraction.

In Figure 9b, the NDD signal is shown next to other modes present in the set of electrodes. Visual inspection allows for a comparison between the NDD mode and transversal

double-differential signals DD_V and DD_H. The gray square to the left in Figure 9b encloses two segments where the addition of these transversal modes to form the NDD is observed. Next, differential signals captured between pairs of electrodes are plotted, $D_{V1} = v_{e2} - v_{e1}$, $D_{V1} = v_{e1} - v_{e4}$, $D_{H1} = v_{e3} - v_{e1}$, and $D_{H2} = v_{e5} - v_{e1}$. The rejection of the NDD signal against the differential signal is evident in the larger gray square to the right in Figure 9b; the enclosed large peaks are not present in the NDD signal.

Table 2 shows an indicative comparison with representative biopotential acquisition systems from the literature [33–35]. The proposed system's operational parameters fall within the reported range of these systems, except for the power consumption, which is higher due to the proof-of-concept discrete implementation. Additionally, the noise performance is notably good considering that NDD measurements require input from five electrodes.

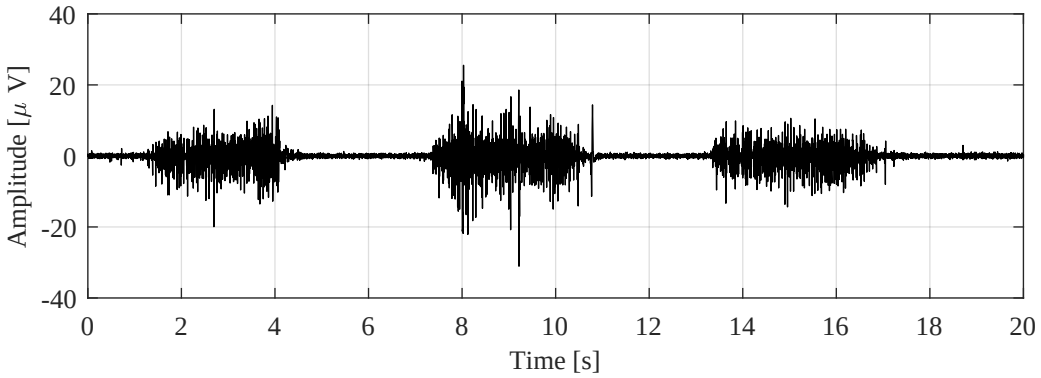

Figure 8. NDD EMG recording.

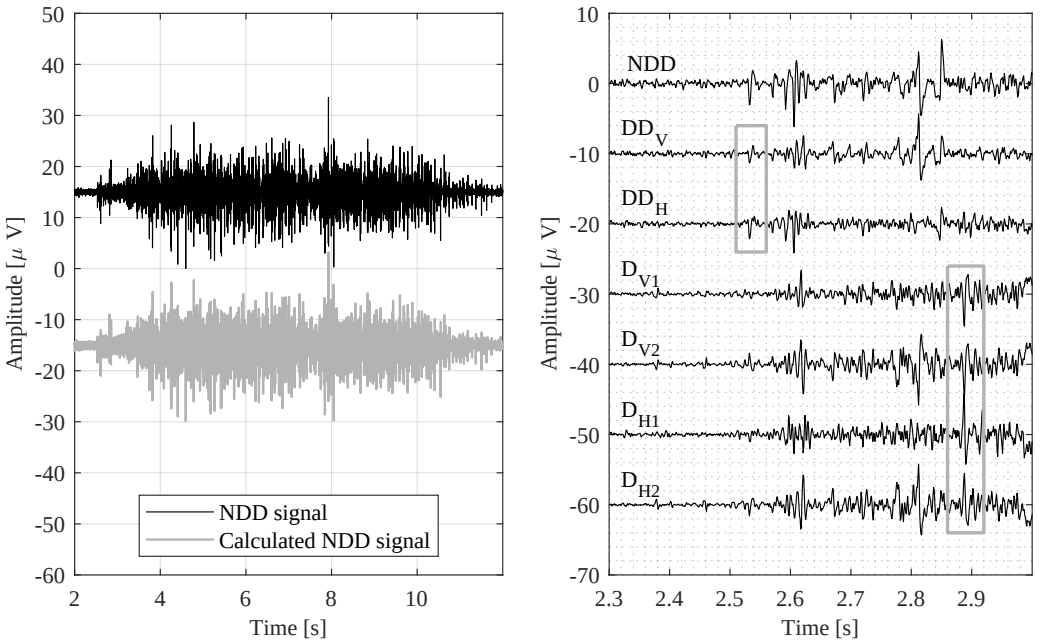

(**a**) (**b**)

Figure 9. NDD function validation. (**a**) NDD amplifier output vs. digitally obtained signal from individual electrodes. The correlation coefficient calculated between 2 and 10 s is 0.98. (**b**) Comparison against captured modes.

Table 2. Parameter comparison with other biopotential measurement front-ends.

Key	CICC'20 [33]	TCAS-I'20 [34]	NorCAS'23 [35]	This Work
Type *	D EMG/ECG	D EMG	4 ch. ExG	NDD EMG
Implementation	ASIC	ASIC	ASIC	Discrete
Noise [μV_{rms}]	3.52	3.45	4.2	3.7
CMRR [dB]	N/A	112	81.6	95.6
Bandwidth [Hz]	1–150	40–320	0.2–512	12–578
Gain [dB]	35	43–55	19.9–53.1	27.9
Supply	1.8 V 43.8 µW	2 V 3.15 µA	1 V 0.56 µW	3.3 V 326 µA
Input impedance	N/A	N/A	216 MΩ @ 10 Hz	2 pF

* D stands for differential; ch. for channels; ExG for general biomedical signals.

4. Final Remarks and Conclusions

This paper proposes a topology that allows for the simple implementation of an NDD electrode, which only uses four voltage buffers and one CCII. To validate and test the topology, a proof-of-concept circuit was realized by using commercial components. In particular, seven OAs were used, five of them to obtain the NDD signal from five electrodes and provide amplification and band-pass filtering and the other two to provide buffering for patient cables. Thus, for the proof-of-concept electrode, only two quad OA OPA4243 integrated circuits were necessary and the design simplicity was confirmed considering that five signals are simultaneously measured and that further analog signal processing is provided.

The derived equations used to design the amplifier and estimate specifications were experimentally validated and the resulting parameters were measured and are presented in Table 1 and Figure 9.

A satisfactory noise model was found for the topology, which showed that the total noise is dependent mainly on the voltage noise of the buffers. Indeed, by using an OPA4243, a 3.7 μV_{rms} noise value was obtained, which, although higher than the figures usually presented for EMG measurements, is appropriate for normal double-differential EMG signals as the noise of five electrodes is compounded. As a benchmark, if the signals from each location were independently measured with five ADC channels, each with the same buffer, the total noise would be

$$e_{n,T} = (4e_n)^2 + \sum_{1}^{4} e_n^2 = 2\sqrt{(5)}\, e_n \tag{22}$$

which, considering (20), shows that the proposed topology has the same noise level as individual buffered measurements that would be found in an array. Both noise and power consumption are closely linked to the noise and power characteristics of the active devices used for the implementation; in this case, they were given by the OPA4243 OAs. However, OAs with different characteristics can be selected, as well as passive components providing gain and filtering, which can be adjusted and optimized according to specific application scenarios following the design equations.

Validation of NDD measurements with the proposed topology was successful, using it as an active electrode. The simultaneous acquisition of signals from the five NDD electrode locations and the electrode's output showed that the NDD function is effectively achieved by the impedance network and measured by the CCII surrogate. Further, according to Figure 9b, the characteristics of the signal modes described in Section 2.1 were observed. The registered signals were selected at the onset of a weak contraction and amplified so as to observe specific features. First, the boxed segments in the top left demonstrate the sum

of the two transversal DD modes in the NDD signal from (3). Then, the high-amplitude peaks from the differential signals in the lower right box are absent in the NDD signal.

In conclusion, the experimental measurements provided validation of the capabilities of the proposed topology to perform the NDD function while achieving sufficient performance parameters for superficial EMG measurements. The circuit resulted in a simple implementation using only two quadruple OAs in the board-level proof of concept. Therefore, thanks to this novel topology, it is feasible to provide an analog front-end for multi-contact EMG active electrodes, including a complete analysis of the relevant rejection ratios.

Author Contributions: Conceptualization, A.D.G., G.P. and F.N.G; Validation, V.A.C.; Investigation, F.N.G.; Writing—original draft, F.N.G.; Writing—review & editing, V.A.C., A.D.G. and G.P.; Supervision, G.P. All authors have read and agreed to the published version of the manuscript.

Funding: This research was funded by Research Projects CONICET PIP-0323, UNLP PID/I254, and PICT INVI 2022-02-00911, Argentina.

Data Availability Statement: The raw data supporting the conclusions of this article will be made available by the authors on request.

Conflicts of Interest: The authors declare no conflicts of interest.

References

1. Casale, R.; Rainoldi, A. Fatigue and fibromyalgia syndrome: Clinical and neurophysiologic pattern. *Best Pract. Res. Clin. Rheumatol.* **2011**, *25*, 241–247. [CrossRef] [PubMed]
2. Jarque-Bou, N.J.; Sancho-Bru, J.L.; Vergara, M. A Systematic Review of EMG Applications for the Characterization of Forearm and Hand Muscle Activity during Activities of Daily Living: Results, Challenges, and Open Issues. *Sensors* **2021**, *21*, 3035. [CrossRef] [PubMed]
3. Zheng, Z.; Wu, Z.; Zhao, R.; Ni, Y.; Jing, X.; Gao, S. A Review of EMG-, FMG-, and EIT-Based Biosensors and Relevant Human–Machine Interactivities and Biomedical Applications. *Biosensors* **2022**, *12*, 516. [CrossRef] [PubMed]
4. Zhao, N.; Zhao, B.; Shen, G.; Jiang, C.; Wang, Z.; Lin, Z.; Zhou, L.; Liu, J. A robust HD-sEMG sensor suitable for convenient acquisition of muscle activity in clinical post-stroke dysphagia. *J. Neural Eng.* **2022**, *20*, 016018. [CrossRef] [PubMed]
5. Lara, J.E.; Cheng, L.K.; Röhrle, O.; Paskaranandavadivel, N. Muscle-specific high-density electromyography arrays for hand gesture classification. *IEEE Trans. Biomed. Eng.* **2021**, *69*, 1758–1766. [CrossRef]
6. Zhu, Z.; Li, J.; Boyd, W.J.; Martinez-Luna, C.; Dai, C.; Wang, H.; Wang, H.; Huang, X.; Farrell, T.R.; Clancy, E.A. Myoelectric Control Performance of Two Degree of Freedom Hand-Wrist Prosthesis by Able-Bodied and Limb-Absent Subjects. *IEEE Trans. Neural Syst. Rehabil. Eng.* **2022**, *30*, 893–904. [CrossRef]
7. Wang, H.; Zuo, S.; Cerezo-Sanchez, M.; Arekhloo, N.G.; Nazarpour, K.; Heidari, H. Wearable super-resolution muscle–machine interfacing. *Front. Neurosci.* **2022**, *16*, 1020546. [CrossRef]
8. Campanini, I.; Merlo, A.; Disselhorst-Klug, C.; Mesin, L.; Muceli, S.; Merletti, R. Fundamental Concepts of Bipolar and High-Density Surface EMG Understanding and Teaching for Clinical, Occupational, and Sport Applications: Origin, Detection, and Main Errors. *Sensors* **2022**, *22*, 4150. [CrossRef]
9. Farina, D.; Arendt-Nielsen, L.; Merletti, R.; Indino, B.; Graven-Nielsen, T. Selectivity of spatial filters for surface EMG detection from the tibialis anterior muscle. *IEEE Trans. Biomed. Eng.* **2003**, *50*, 354–364. [CrossRef]
10. Dimitrov, G.V.; Disselhorst-Klug, C.; Dimitrova, N.a.; Schulte, E.; Rau, G. Simulation analysis of the ability of different types of multi-electrodes to increase selectivity of detection and to reduce cross-talk. *J. Electromyogr. Kinesiol.* **2003**, *13*, 125–138. [CrossRef]
11. Germer, C.M.; Farina, D.; Elias, L.A.; Nuccio, S.; Hug, F.; Del Vecchio, A. Surface EMG cross talk quantified at the motor unit population level for muscles of the hand, thigh, and calf. *J. Appl. Physiol.* **2021**, *131*, 808–820. [CrossRef] [PubMed]
12. Prasad, S.; Paulin, M.; Cannon, R.D.; Palla, S.; Farella, M. Smartphone-assisted monitoring of masticatory muscle activity in freely moving individuals. *Clin. Oral Investig.* **2019**, *23*, 3601–3611. [CrossRef]
13. Zadeh, S.M.; MacDermid, J.; Johnson, J.; Birmingham, T.B.; Shafiee, E. Applications of wearable sensors in upper extremity MSK conditions: A scoping review. *J. NeuroEng. Rehabil.* **2023**, *20*, 158. [CrossRef]
14. Alizadeh-Meghrazi, M.; Sidhu, G.; Jain, S.; Stone, M.; Eskandarian, L.; Toossi, A.; Popovic, M.R. A Mass-Producible Washable Smart Garment with Embedded Textile EMG Electrodes for Control of Myoelectric Prostheses: A Pilot Study. *Sensors* **2022**, *22*, 666. [CrossRef]
15. Kinugasa, R.; Kubo, S. Development of Consumer-Friendly surface electromyography system for muscle fatigue detection. *IEEE Access* **2023**, *11*, 6394–6403. [CrossRef]
16. Tam, S.; Bilodeau, G.; Brown, J.; Gagnon-Turcotte, G.; Campeau-Lecours, A.; Gosselin, B. A Wearable Wireless Armband Sensor for High-Density Surface Electromyography Recording. In Proceedings of the 2019 41st Annual International Conference of the IEEE Engineering in Medicine and Biology Society (EMBC), Berlin, Germany, 23–27 July 2019; pp. 6040–6044. [CrossRef]
17. Reis Carneiro, M.; Majidi, C.; Tavakoli, M. Multi-Electrode Printed Bioelectronic Patches for Long-Term Electrophysiological Monitoring. *Adv. Funct. Mater.* **2022**, *32*, 2205956. [CrossRef]

18. Al-Ayyad, M.; Owida, H.A.; De Fazio, R.; Al-Naami, B.; Visconti, P. Electromyography Monitoring Systems in Rehabilitation: A Review of Clinical Applications, Wearable Devices and Signal Acquisition Methodologies. *Electronics* **2023**, *12*, 1520. [CrossRef]
19. Lee, S.; Yoon, J.; Lee, D.; Seong, D.; Lee, S.; Jang, M.; Choi, J.; Yu, K.J.; Kim, J.; Lee, S.; et al. Wireless Epidermal Electromyogram Sensing System. *Electronics* **2020**, *9*, 269. [CrossRef]
20. Kawano, T.; Koganezawa, K. A method of discriminating fingers and wrist action from surface EMG signals for controlling robotic or prosthetic forearm hand. In Proceedings of the 2016 IEEE International Conference on Advanced Intelligent Mechatronics (AIM), Banff, AB, Canada, 12–15 July 2016; IEEE: Banff, AB, Canada, 2016; pp. 13–18. [CrossRef]
21. Pizzolato, S.; Tagliapietra, L.; Cognolato, M.; Reggiani, M.; Müller, H.; Atzori, M. Comparison of six electromyography acquisition setups on hand movement classification tasks. *PLoS ONE* **2017**, *12*, e0186132. [CrossRef]
22. Garcia-Casado, J.; Ye-Lin, Y.; Prats-Boluda, G.; Makeyev, O. Evaluation of Bipolar, Tripolar, and Quadripolar Laplacian Estimates of Electrocardiogram via Concentric Ring Electrodes. *Sensors* **2019**, *19*, 3780. [CrossRef]
23. Catacora, V.A.; Guerrero, F.N.; Spinelli, E.M. Three-Electrode Double-Differential Biopotential Amplifier for Surface EMG Measurements. *IEEE Trans. Instrum. Meas.* **2023**, *72*, 2003508. [CrossRef]
24. Samani, A.; Srinivasan, D.; Mathiassen, S.E.; Madeleine, P. Variability in spatio-temporal pattern of trapezius activity and coordination of hand-arm muscles during a sustained repetitive dynamic task. *Exp. Brain Res.* **2017**, *235*, 389–400. [CrossRef] [PubMed]
25. Messaoudi, N.; Bekka, R.E.; Belkacem, S. Classification of the Systems Used in Surface Electromyographic Signal Detection according to the Degree of Isotropy. *Adv. Biomed. Eng.* **2018**, *7*, 107–116. [CrossRef]
26. Guerrero, F.N.; Spinelli, E.M.; Grasso, A.D.; Palumbo, G. Double-Differential Amplifier for sEMG Measurement by Means of a Current-Mode Approach. *IEEE Access* **2022**, *10*, 45870–45880. [CrossRef]
27. Smith, K.C.; Sedra, A. The Current Conveyor*—A New Circuit Building Block. *Proc. IEEE* **1968**, *56*, 1368–1369. [CrossRef]
28. Sedra, A.; Smith, K.C. A Second-Generation Current Conveyor and Its Applications. *IEEE Trans. Circuit Theory* **1970**, *17*, 132–134. [CrossRef]
29. Huhta, J.C.; Webster, J.G. 60-HZ interference in electrocardiography. *IEEE Trans. Bio-Med Eng.* **1973**, *20*, 91–101. [CrossRef]
30. Guerrero, F.N.; Spinelli, E.M.; Haberman, M.A. Analysis and simple circuit design of double differential EMG active electrode. *IEEE Trans. Biomed. Circuits Syst.* **2015**, *10*, 787–795. [CrossRef] [PubMed]
31. Koli, K.; Halonen, K.A. CMRR enhancement techniques for current-mode instrumentation amplifiers. *IEEE Trans. Circuits Syst. I: Fundam. Theory Appl.* **2000**, *47*, 622–632. [CrossRef]
32. Pu, J.; Ma, K.; Luo, Y.; Tang, S.; Liu, T.; Liu, J.; Leung, M.; Yang, J.; Hui, R.; Xiong, Y.; et al. Textile electronics for wearable applications. *Int. J. Extrem. Manuf.* **2023**, *5*, 042007. [CrossRef]
33. Kim, J.; Ouh, H.; Johnston, M.L. A 43.8 µW per Channel Biopotential Readout System using Frequency Division Multiplexing with Cable Motion Artifact Suppression. In Proceedings of the 2020 IEEE Custom Integrated Circuits Conference (CICC), Boston, MA, USA, 22–25 March 2020; IEEE: Piscateville, NJ, USA, 2020; Volume 2020-March , pp. 1–4.
34. Hsu, Y.P.; Liu, Z.; Hella, M.M. A -68 dB THD, 0.6 mm2 Active Area Biosignal Acquisition System with a 40-320 Hz Duty-Cycle Controlled Filter. *IEEE Trans. Circuits Syst. I Regul. Pap.* **2020**, *67*, 48–59. [CrossRef]
35. Fath, P.; Pretl, H. A 370-nW Quad-Channel Multi-Mode Bio-Signal Acquisition AFE with 2.9-μVrms Input Noise. In Proceedings of the 2023 IEEE Nordic Circuits and Systems Conference (NorCAS), Aalborg, Denmark, 31 October–1 November 2023; IEEE: Piscateville, NJ, USA, 2023; pp. 1–5.